Check for updates

Creating chirality in WSe$_2$ through screw dislocations by chemical vapor transport†

Philip Putze, [ID] *[a] Tobias Ritschel,[b] Paul Chekhonin,[c] Jochen Geck,[b] Daniel Wolf,[a] Alexey A. Popov, [ID] [a] Bernd Büchner,[ab] Peer Schmidt [ID] [d] and Silke Hampel [ID] *[a]

Screw dislocation-driven nanostructures of two-dimensional transition metal dichalcogenides (2D TMDs) can feature chirality that enables prominent asymmetric optical properties. One of the outstanding representatives is WSe$_2$ as it can exhibit intriguing new size and shape-dependent chemical and physical properties compared to its bulk counterpart. Crystal growth control in nanostructures with screw dislocation-driven growth is central for exploiting their structure-related properties. However, bottom-up syntheses of 2D TMDs usually contain 'trial and error' approaches. Here we report on the rational synthesis planning and realizing for the binary system W:Se to achieve chirality in nano-scale crystals by chemical vapor transport (CVT). For that purpose, key parameters were modelled based on thermodynamic datasets. Thus, crystal growth by CVT under addition of SeCl$_4$ succeeds for right-handed spiral nanocrystals from 850 °C to 800 °C with a dwell time of 60 min, while left-handed spirals are obtained from 915 °C to 860 °C. Surface-fused SiO$_2$ nanoparticles on an Si(100) substrate served as potential nucleation points. Chirality of screwed WSe$_2$ was unprecedentedly investigated by circular-polarized Raman Spectroscopy and showed an intensity increase of the E$_{2g}^1$ mode of 29% and 15% for right and left-handed spirals, respectively. Pyramid-like WSe$_2$ analyzed by atomic force microscopy exhibits step heights of around 10 nm. Electron backscatter diffraction patterns reveal a convex curvature for WSe$_2$ with the curvature radii determined as R_x = (270 ± 32) μm and R_y = (141 ± 9) μm, respectively.

New concepts

Chirality in screwed nanostructures in two-dimensional transition metal dichalcogenides unlocks remarkable asymmetric optical characteristics, making them highly desirable for advanced applications. We introduce a pathway to create chirality through screw dislocation-driven growth in nano-WSe$_2$ by chemical vapor transport. Usually, the majority of vapor pressure-assisted synthesis routes contain 'trial and error' approaches. Note that our concept is based on thermodynamic modelling to directly determine the optimum temperature ranges and the amount of starting materials, and thus avoid empirical procedures. Low supersaturation linked to optimum synthesis conditions enables left and right-handed spiral stacking geometries that exhibit step heights of around 10 nm. Through circularly polarised Raman spectroscopy, we confirm the differences in chirality linked to an intensity increase of at least 15% of the active E$_{2g}^1$ mode, which is until now unprecedented. Furthermore, as-grown highly crystalline WSe$_2$ exhibits varying curvature radii determined by electron backscatter diffraction patterns. In summary, the application of thermodynamic simulations opens up a pathway to create chirality in nanocrystals for similar material systems.

Introduction

Unprecedented attention in research towards two-dimensional (2D) materials has been gradually garnered since 2004 as experimental identification and systematic characterization marked the beginning of research of this new compelling materials class.[1] All 2D materials open up an ideal platform for creating artificial structures featuring intriguing and peculiar properties by stacking different layers vertically.[2,3] Complementary to the semi-metallic electronic properties of graphene, 2D transition metal dichalcogenides, henceforth referred to as TMDs, with the generally applied formula of MX_2 (M = Mo, W; X = S, Se, Te) exhibit a finite bandgap which results in unique structural,[4] magnetic[5] and optoelectronic[6,7] properties. One of the outstanding representatives is tungsten diselenide WSe$_2$. For instance, the thermal conductivity differs between the

[a] Leibniz Institute for Solid State and Materials Research, Institute for Solid State Research, Helmholtzstraße 20, 01069 Dresden, Germany. E-mail: p.putze@ifw-dresden.de, s.hampel@ifw-dresden.de

[b] Institute of Solid State and Materials Physics, Department of Physics, TUD Dresden University of Technology, Haeckelstraße 3, 01069 Dresden, Germany

[c] Helmholtz-Zentrum Dresden-Rossendorf, Institute of Resource Ecology, Bautzner Landstraße 400, 01328 Dresden, Germany

[d] Brandenburg University of Technology (BTU) Cottbus – Senftenberg, Chair of Inorganic Chemistry, Universitätsplatz 1, 01968 Senftenberg, Germany

monolayer and the bulk system with 3.935 W m^{-1} K^{-1} and 17 W m^{-1} K^{-1}, respectively.[8,9] Bulk-WSe$_2$ is stated as the p-type semiconductor and exhibits an indirect bandgap in the visible range of ≈ 1.20 eV, while monolayer WSe$_2$ provides a direct bandgap of ≈ 1.39 eV at 300 K.[10] WSe$_2$ exhibits a well-described structure given a layer thickness of ≈ 0.7 nm with layers bonded by weaker interlayer forces that are of inherently nonlocal van-der-Waals nature.[11] Several structural phases of WSe$_2$ result from different coordination spheres of the transition metal atoms. Commonly encountered polymorphs are characterized by either the trigonal prismatic (2H, space group $P6_3/mmc$)[12] or octahedral (1T, space group $P\bar{3}m1$)[13] crystal coordination. Additionally, tuning the twist angles between stacked bilayers has been identified as an interesting degree of freedom, which avoids challenging chemistry of (hetero)-structures and thereby offers to fine-tune exotic correlated electronic states,[14] e.g., unconventional superconductivity,[15] tunable Mott insulators[15,16] and Moiré excitons.[17,18] Computational studies for twisted materials were constraint to systems with twist angles at 7.34° and 67.34° with respect to Moiré flat-band systems.[19] To achieve twisted structures based on a chemical point of view, the dislocation-driven growth contains screw dislocation defects that provide self-perpetuating growth steps. These steps, then, allow the anisotropic growth. One essential prerequisite is the low supersaturation condition. The growth rate of crystal growth modes can be viewed as a function of the supersaturation.[20] Beyond screw dislocations on non-Euclidean surfaces, chiral inorganic structures have attracted a great deal of attention as chirality of the crystals can sufficiently alter their characteristic properties.[21–25] Recent studies pin-point to a broad range of materials, e.g., 4H-SiC,[26] helical nanotube structures of MoS$_2$,[27] NiMoO$_4$,[28] and hexagonal crystalline platelets.[29] Chirality in materials enables second-order optical nonlinearity[30] and chiral-induced spin selectivity[31] as well as topological transport.[32]

For the synthesis of WSe$_2$ crystals, bottom-up approaches such as chemical vapor-assisted methods are employed. Bulk-WSe$_2$ crystals have predominantly been prepared by the classic chemical vapor transport (CVT) method, using both well-established transport additions such as Se(s),[33] Br$_2$(l)[33,34] and I$_2$(s)[35] as well as chlorinating additions such as SeCl$_4$(s)[33] and TeCl$_4$(s).[36] Regardless of the bulk material, thin films of WSe$_2$ were achieved by atmospheric pressure chemical vapor deposition (CVD).[37] Based on the flat structures, screw dislocation-driven nanomaterials were only synthesized using a CVD set up. Thus, few-layer and pyramid-like WSe$_2$ were synthesized by sulfur-assisted CVD,[38] while spiral growth was achieved by CVD with NaCl(s) acting as a co-solvent.[39] A closer look at the literature on controlled growth of screw dislocation-driven crystals, however, reveals a number of knowledge gaps as nanostructures with those characteristics have not been reported yet for the classic CVT set-up. Questions to be addressed are how to evade 'trial and error' approaches in the CVT synthesis for a rational crystal growth design[40] and which temperature ranges are appropriate to achieve chiral nano-WSe$_2$ crystals.

Herein, the key focus is set on the binary system W/Se investigated with regard to a rational approach of planning and realizing of a bottom-up synthesis of chiral WSe$_2$ nanocrystals with screw dislocations. Therefore, the frame parameters of the CVT experiments are based on thermodynamic modelling of the reaction according to CalPhaD (calculation of phase diagrams) methods. This study addresses several further questions on how the applied temperature affects the screw dislocation-driven growth in terms of topography characteristics, and the change of orientation in the direct environment of the screw dislocation zones compared to a reference system. We show WSe$_2$ nanostructures with different chiralities can be realized and were investigated by TEM, AFM and EBSD, while the chiralities of crystals have been verified by Raman spectroscopy. Thus, rational synthesis routes ascended as essential in order to realize desirable dimensionalities and the respective morphologies.
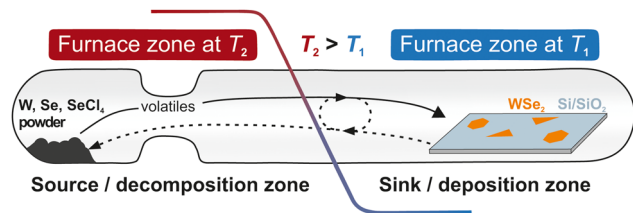
Experimental section

Thermodynamic simulations using TRAGMIN software

In order to determine optimum reaction conditions, the vapor transport of the W:Se system was modelled initially. For that purpose, CalPhaD methods were applied. Thermodynamic modelling experiments were performed by the TRAGMIN software V. 5.2 for both single equilibrium room arrangement and two-room model linked equilibrium spaces of dissolution and deposition.[41] Partial pressures for the species were calculated in a wide temperature range and finally evaluated for the relevant range of 800 °C $\leq \vartheta \leq$ 850 °C. Simulations were performed by using an equidistant gradient of $\Delta T = 5$ K between each step. The constant volume of $V = 9.4$ mL corresponds to the real experimental ampoule dimensions. For all modelling experiments, a framework of parameters was set. In order to represent actual experimental conditions, a small amount of Argon was used as the inert/reference gas: $n(\text{Ar}) = 10^{-6}$ mmol, and traces of moisture/oxygen were set with $n(\text{H}_2\text{O}) = 10^{-5}$ mmol. Selenium tetrachloride SeCl$_4$(s) was used as transport addition with $n(\text{SeCl}_4) = 0.004$ mmol. With respect to the use of SeCl$_4$(s), the stoichiometric ratio between W and Se was set as W : Se = 1 : 2001. Thermodynamic data of all entities used for simulations and information considering the calculation of the transport efficiency are enlisted in the ESI.†

Preparation of the ampoules

Oxygen- and moisture-sensitive starting materials and the products of the synthesis for the bulk materials were stored in an argon-filled MB 200B Eco glovebox (M Braun; $p(\text{H}_2\text{O})/p° <$ 1 ppm and $p(\text{O}_2)/p° <$ 1 ppm). Tungsten W powder (abcr, 99.95%) and selenium Se powder (Alfa Aesar, 99.999%) were weighed and thoroughly ground to prepare a mixture according to the stoichiometric ratio of W:Se = 1:2. For the bulk material, (40 ± 1) mg of the mixture from the elements and (2 ± 1) mg of SeCl$_4$(s) powder (Sigma Aldrich, 99.999%) were weighed and funneled in a one-chamber silica glass ampoule.

Fig. 1 Concept of the experimental work-up of the CVT experiment using a two-chamber silica glass ampoule. Starting materials are placed on the source side (T_2) and the SiO$_2$@Si(100) substrate is positioned on the sink side (T_1), with $T_2 > T_1$. An applied temperature gradient is given as the red line.

No pre-reaction of the components was necessary before the actual transport experiments. Synthesis for the WSe$_2$ nanostructures was performed with (5 ± 1) mg of the mixture and (1 ± 0.5) mg of the SeCl$_4$(s) powder that were funneled in the source side of a two-chamber silica glass ampoule (diffusion distance: $d_a \approx 12$ cm, inner diameter: $d_i \approx 10$ mm, inner taper diameter: $d_{i,t} \approx 5.3$ mm), see Fig. 1. Additionally, approaches with pre-synthesized WSe$_2$ were conducted; nevertheless, screwed nanostructures could not be obtained. In order to force the materials to form screw dislocation-driven growth, SiO$_2$ nanoparticles were seeded on a Si(100) substrate (ESI†). Subsequently, a standard Schlenk-line ($p = 1.0 \times 10^{-3}$ mbar) was employed for sealing. The source side was additionally cooled by a woven fabric saturated in liquid nitrogen in order to avoid early evaporation of starting materials.

Chemical vapor transport experiments

CVT experiments were conducted using a horizontally mounted LOBA two-zoned Tube Furnace (HTM Reetz). For a quantitative transport, the mixture for the bulk synthesis was thermally treated from 900 °C to 820 °C with a heating rate of $\beta = 10$ K min^{-1} towards the temperature gradient targeted and a dwell time of $t_{dwell} = 72$ h. Subsequently, the ampoules were quenched with water. Nanostructures were synthesized from 850 °C to 800 °C with a heating rate of $\beta = 10$ K min^{-1} towards the temperature gradient aimed and an applied dwell time of $t_{dwell} = 60$ min. Consequently, ampoules were first cooled on the source side in order to avoid contamination of the crystals grown and stored in the glovebox. Upon cooling in air or quenching with water, crystals appeared in a similar shape which leads to the assumption that quenching has no effect on the result.

Characterization of the as-grown crystals

Powder X-ray diffraction (pXRD). To achieve the identification of the bulk crystals synthesized during the CVT process and to aim clarification about phase purity, powder X-ray diffractograms were recorded. Bulk material was ground thoroughly, and fixed with collodion glue on an X-ray amorphous polyacetate foil. pXRD was performed on a Stadi P Dual Source Diffractometer (STOE) in the Bragg–Brentano geometry. Experiments were performed in a diffraction angle range of $10° \leq 2\theta \leq 120°$ with a step size of 0.015° and 60 s per step.

Measurements were conducted in transmission mode at room temperature. Cobalt served as radiation source $\lambda(\text{Co } K_{\alpha1}) = 1.788965$ Å. A curved Ge(111) primary beam monochromator and a nickel filter were applied. A semiconducting MYTHEN 1 K strip detector (1280 strips) was used. An acceleration voltage of $U_a = 40$ kV and a filament current of $I = 10$ mA were utilized. pXRD patterns were analyzed using the WinX^{POW} software V. 3.12.4. For identification, reference samples based on the ICSD database (Inorganic Crystal Structure Database) were used.

Light microscopy. Morphology and habitus of the as-grown crystals in nanoscale and bulk materials were analyzed with a light microscope. Images of the as-grown bulk samples in the sealed ampoules were immediately taken after quenching with a Leica Microscope M80 (Leica) equipped with a Leica MC170 HD camera. The LAS software V. 4.8 was used. Microscopic investigations of the as-grown nanoparticles were performed using a KEYENCE VHX-7000 Digital Microscope (Keyence) with a VHX-7020 high-performance camera with a CMOS image sensor and several objectives to adjust the magnification (Keyence VHX-E series) under ambient conditions. Images were taken from the VHX software V. 2.3.16.295.

Scanning electron microscopy (SEM) and energy-dispersive X-ray (EDX) analysis. Analytical scanning electron microscopy (SEM) of the as-grown crystals was recorded using a NOVA NanoSEM 200 (FEI Company) device, which facilitated vacuum conditions to analyze the WSe$_2$ surface properties. Substrates were scattered on a double-sided carbon tape that was glued on an aluminum stub ($d \approx 10$ mm). Secondary electrons were detected using an Everhart–Thornley detector. All samples were analyzed with a secondary electron detector with an applied acceleration voltage between 5 kV and 15 kV. Experiments were conducted in standard operational mode at high magnifications. Elemental analysis was performed by the EDX that is built into the SEM and analyzed by the EDAX Genesis Spectrum software V. 6.32. The energetic resolution was set to be 10 eV, and the detection limit was >1 wt%. The EDAX Genesis Spectrum software V. 6.32 directly calculated the relative elemental composition.

Focused ion beam (FIB) lamella preparation. Cross-sectioning and high-resolution imaging on both the SiO$_2$@Si(100) substrates and FIB lamella of WSe$_2$ crystals were conducted with a Helios 5 CX (Thermo Scientific). As a protective layer for the crystals selected, a C/Pt cover was applied for the cutting. The cutting process was executed by using an acceleration voltage of $U_a = 30$ kV. Gallium was used as the ion beam source. The milling current was set at $I = 86$ pA and the milling depth was $d_m \approx 8$ μm. Images were taken in the SE-mode and exhibit a tilt-corrected scale bar. The acceleration voltage for the SEM images was $U_a = 3$ kV.

High-resolution transmission electron microscopy (HR-TEM). Cross-sectional aberration-corrected HR-TEM of the FIB lamella was performed with a C_s-corrected FEI Titan^3 80–300 transmission electron microscope (ThermoFisher Company) at an acceleration voltage of 300 kV. To index the reflections of the diffractograms, the Single-Crystal software V. 3.1.5 (CrystalMaker Software Ltd) was used.

Electron backscatter diffraction (EBSD). To obtain crystallographic information about the WSe$_2$ samples, EBSD was utilized. EBSD measurements were performed in an Ultra 55 SEM (Carl Zeiss AG) equipped with a Nordlys EBSD system (HKL Technology A/S). The measurements were done with a tilt angle of $\theta = 70°$ at an acceleration voltage of $U_a = 10$ kV and a sample current of $I = 0.5$ nA. The step size was set to 0.5 μm in a rectangular grid. EBSD acquisition as well as data evaluation were performed using the Channel 5 software V. 5.0.9.0 (HKL Technology A/S).

Atomic force microscopy (AFM). Spiral stacking morphologies were characterized using an AFM icon Dimension NanoScope 9.1 (Bruker) in a standard tapping mode in air. An etched Si single-crystal was used as a cantilever with a spring constant of $k = 3$ N m^{-1}. Measurements were conducted with an Olympus AC 160TS-R3 tip. For each image, the scan rate was set to be 0.5 Hz, the drive amplitude was set to be ≈ 100 mV and 1024 samples per line were taken. To characterize the thickness and surface topography of the crystals, the NanoScope Analysis software V. 1.8 was used. Suitable crystals were pre-selected using optical microscopy under ambient conditions.

Raman spectroscopy. Raman spectra were recorded using a Raman Spectrometer T64000 (Horiba Scientific) in the range of 700 cm^{-1} < $\tilde{\nu}$ < 50 cm^{-1} at room temperature. As the excitation source, a 660 nm linear-polarized torus laser (Laser Quantum) with a spot size of 1 μm was applied. The maximum power was chosen to avoid destruction of the sample and the grating used was 1800 g mm^{-1}. A 50× Mplan N objective (Olympus) with an aperture of 0.75 was used. A Symphony II 2048 × 512 Cryogenic Back-Illuminated CCD detector (400 nm < λ < 1000 nm) was used. The device was calibrated using Si–I with the main peak at $\tilde{\nu} = 520.2$ cm^{-1}. Analyses of the Raman spectra were performed with the Labspec 6 software. A scheme of the spectrometer and information about circularly polarized Raman measurements are given in the ESI.†

Results and discussion

Rational design of crystal growth by modelling of CVT

Thermodynamic modelling was used as a tool to render 'trial and error' approaches for the W/Se/Cl system with a tightened temperature window for essential CVT parameters, such as temperature and the temperature gradient. For this, TRAGMIN simulations allowed bridging theoretical considerations through modelling with experimental methods by chemical vapor precipitation. Based on considerations regarding the ternary phase diagram W/Se/Cl and respective stationary simulations of complex equilibria, the conditions for the endothermic CVT with respect to the temperature and temperature gradient as well as the reaction system composition were chosen to be in the range 800 °C $\leq \vartheta \leq$ 850 °C (ESI†). Additionally, small excess of selenium species is essential in order to enhance the activity of Se(g) during the crystal growth process that can be realized by the addition of SeCl$_4$(s). Here, SeCl$_4$(s) is the initial experimental addition, while the actual active species and thus also the transport agent are formed in subsequent equilibria. The gaseous species WCl$_4$(s), Se$_2$(g) and SeCl$_2$(g) then become relevant for the transport, while the formation of HCl(g) results from the assumption of experimental conditions that cannot completely avoid the presence of traces of water or moisture. Other oxygen-containing species, such as SeO(g), SeO$_2$(g), and WO$_2$(g) are non-effective in a realistic experimental scenario ($p_i < 10^{-26}$ bar), see Fig. 2. That is, no oxidic contamination should be precipitated at the crystallization site. Finally, a formal dominating transport equation concludes eqn (1).

$$\text{WSe}_2(\text{s}) + 2\text{SeCl}_2(\text{g}) \rightleftharpoons \text{WCl}_4(\text{g}) + 2\text{Se}_2(\text{g}) \tag{1}$$

An allocation of essential parameters for the evaluation of the CVT experiments is given by Table 1.
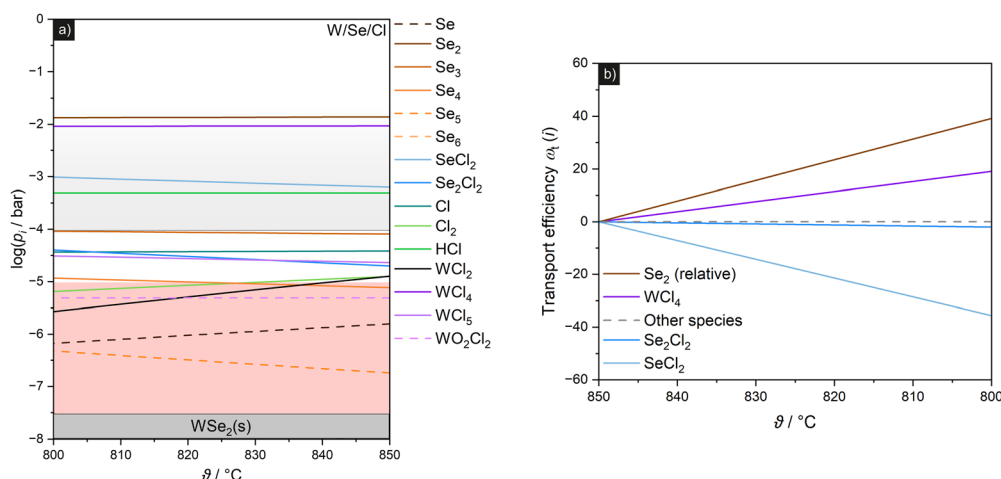
Fig. 2 Simulation of the partial pressure behavior in a sealed ampoule. (a) Partial pressure for different gas species in the temperature range of 800 °C $\leq \vartheta \leq$ 850 °C for an endothermic CVT. Area for log(p_i) > −4 is marked grey. Non-effective pressure area for $p \leq 10^{-5}$ bar is marked red with species shown as the dashed line. Condensed phases shown as the dark grey rectangle. (b) Calculated transport efficiency $\omega_t(i)$ for the temperature range given. $\omega_{t,rel}$(Se$_2$) corresponds to the homogeneous equilibria in the gas phase for Se$_w$ species.

Table 1 Essential CVT parameters for bulk and nano-WSe$_2$ as simulated by TRAGMIN. Two-room modelling represents simulations for the CVT. Calculated transport rates are given by $\dot{m}_{calc.}$.

| Material	Modell	$n(i)$/mmol			ϑ_{source}/°C	ϑ_{sink}/°C	ΔT/K	$\dot{m}_{calc.}$/mg h^{-1}	Boundary phases
		W	Se^a	Cl					
Bulk	Two room	1	2.001	0.002	1900	820	80	3.36	—
Nano	Two room	1	2.001	0.004	1915	860	55	1.63	—
Nano	Two room	1	2.001	0.004	1890	840	50	1.61	—
Nano	Two room	1	2.001	0.004	1850	800	50	2.15	—

^{a} Excess for two-room modelling related to addition of SeCl$_4$(s).

Synthesis and characterization of bulk-WSe$_2$

The CVT process for the bulk material was conducted based on the modelling data acquired by TRAGMIN to achieve WSe$_2$ crystals that serve as the reference material (ESI†). Optimized synthesis parameters correspond to the quantitative transport from 900 °C to 820 °C. Bulk-WSe$_2$ crystals show predominantly a hexagonal shape. Crystals occur in slightly varying size, see Fig. 3(a) and (b). Smaller particles on the bulk-WSe$_2$ crystals can derive from broken larger crystals during the sample preparation. SEM images underline the variety in the crystal shape, see Fig. 3(c)–(e). pXRD analysis gives a strong hint for phase purity of the pre-synthesized WSe$_2$, see Fig. 3(f). Reflexes that appear within the diffraction angle range $10° \leq 2\theta \leq 120°$ can all be attributed to the 2H modification. The main reflex at $36.6°$ (2θ) is associated with the preferred (100) orientation. All other reflexes in the diffractogram are in accordance with hexagonal primitive 2H-WSe$_2$ (ICSD: 40752, space group: $P6_3/mmc$).[42] Complementary to pXRD, EDX analyses reveal a stoichiometric ratio of the elements of W : Se = 1 : 2, see Fig. 3(g).

Synthesis and characterization of crystals with screw dislocations

Surface morphology. The rational bottom-up crystal growth corresponds to thermodynamic modelling and led to conditions that resulted in spiral stacking crystals. Triangular and hexagonal pyramid-like crystals were yielded with concomitant formation of irregularly shaped WSe$_2$ crystals within three proper temperature windows for screw dislocation-driven growth, namely 915 °C → 860 °C, 890 °C → 840 °C and 850 °C → 800 °C. In contrast to that, experiments without seeded SiO$_2$ nanoparticles, *i.e.*, on a flat substrate resulted in only flat crystals. Surface-fused SiO$_2$ nanoparticles serve as potential nucleation points for the crystal growth. These take up the role as defects on the substrate and affect (lower) the surface energy on the substrate. Thus, substrates with seeded nanoparticles resulted in screw dislocated WSe$_2$ particles. Compared to the formed crystals during the open-system CVD[43,44] in which the growth is affected by the continuous gas flow, the closed-system CVT in this study generally contains certain equilibria in both the gas phase and between the gas
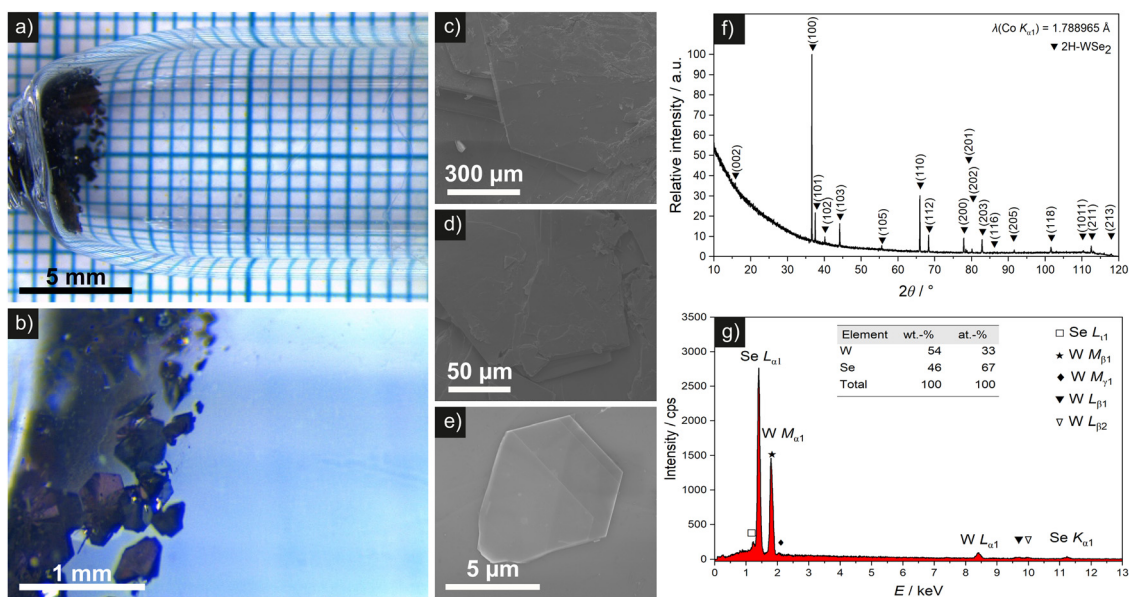
Fig. 3 Bulk-WSe$_2$ crystals synthesized by CVT. (a) and (b) Light microscopy images from the as-grown crystals on the sink side of the ampoule and of selected crystals showing a shiny surface. (c)–(e) SEM images showing flat, hexagonally shaped WSe$_2$ crystals. (f) pXRD pattern of bulk-WSe$_2$ within the diffraction angle range $10° \leq 2\theta \leq 120°$, λ(Co K$_{\alpha1}$) = 1.788965 Å. Measured in transmission mode. WSe$_2$ reference based on the ICSD database. (g) EDX analysis indicating an elemental ratio of W : Se = 1 : 2.

phase and over the solid. Hexagonally shaped WSe_2 were formed with a distinct symmetry with angles of $\approx 120°$ at the crystal edges, see Fig. 4(a)–(d). The elemental ratio was confirmed by EDX analysis (ESI†). Cross-sectional HR-TEM analysis of a fabricated FIB lamella (Fig. 4(e)) confirms that as-grown WSe_2 nanostructures represent the 2H phase. Representative HR-TEM images taken in the [100] zone axis orientation shown in Fig. 4(f)–(g) reveal the layered atomic arrangement along the c-axis, which is characteristic to the 2H structure.[12] Lattice parameters of $a = 3.291$ Å and $c = 13.06$ Å of the 2H modification were obtained from the measured lattice fringe spacings in the HR-TEM micrographs which agree very well with the literature values.[42] Remarkably, we also observed atomic steps of the WSe_2 crystals at the interface to the oxidized silicon substrate as highlighted with green lines in Fig. 4(f). Additionally, Fig. 4(g) displays a cross-sectional cut through a 10 nm step at the surface of the WSe_2, gradually changing within the 25 nm range and including a crack due to stacking faults. Fourier transform (FT, diffractogram) of Fig. 4(g) depicted in (h) can be indexed corresponding to the [100] zone axis of the hexagonal 2H-WSe_2. The lattice plane distance d_{010} was determined to be 2.85 Å again consistent with the assumed crystal structure.

An important question associated with the pyramidal growth is how the crystal orientation is affected at the screw dislocation zones. Subsequently, EBSD was applied to initially analyze the as-grown WSe_2 on the substrate without time-consuming sample preparation. Experimental data were fit with theoretical structure parameters from both the 2H and 1T-bulk reference. Hence, Kikuchi lines were indexed, see Fig. 5. Generally, the EBSD pattern fits with both modifications. However, in the case of 1T-WSe_2 it appears that some few of the simulated Kikuchi bands do not fit the observed lines. Thus, EBSD suggests a better fit with the 2H structure type. Considering the bulk synthesis under similar growth conditions, the fitting provides a complementary identification to the pXRD data. This can be taken qualitatively to indicate good crystallinity. Interestingly, further characterization revealed an observable pattern shift along the horizontal as well as the vertical orientations across the sample (ESI†). This orientation change indicates a convex curvature of the sample morphology. The pattern shifts measured at the [001] zone axis via cross correlation result in a horizontal pattern shift of $S_x = (0.362 \pm 0.039)$ mm. With respect to the pattern on the top and bottom of the sample, the vertical pattern shift of $S_y = (0.626 \pm 0.024)$ mm is noteworthily larger than along the horizontal and thus corresponds to a convex curvature. The curvature radii were determined as $R_x = (270 \pm 32)$ μm and $R_y = (141 \pm 9)$ μm, respectively. Any orientation change can be induced either by plastic deformation via dislocations or by elastic strain/strain relaxation at boundaries.[45]

Topography and classification by AFM. Screw dislocation-driven growth was investigated with the intention for a more profound quantitative analysis. Previous studies stated spiral growth is most favorable under low supersaturation conditions.[46,47] Key parameters of step height (h), terrace width (w) and slope (s) allow a more quantitative description according to eqn (2). Hence, growth conditions can be mirrored at a certain degree.

$$s = \frac{h}{w} \qquad (2)$$

Height profiles depict symmetric hexagonally shaped crystals with a height of $h \approx 370$ nm, see Fig. 6. Each individual step is around 10 nm and all height plateaus are of comparable size. The crystals exhibit the same angles of $60°$ at the corners of the screw dislocation, while at the outer zones the dislocation spirals emerge with angles slightly higher than $120°$ similar to that described by Shearer et al.[48] Geometry is the origin of aligned spirals with Euclidean geometry governing the translational symmetry of the WSe_2 crystal lattice.[43,44] Thus, the fixed angle between two adjacent edges by crystallographic indices[49] and the sum of the measures of the exterior angles which is $360°$ are two geometric properties.[50] This is referred to any convex polygon.[51] Layered WSe_2 shows the shear along the out-of-plane direction and exhibits a continuous layer. The Eshelby twist[52] as the stress effect can be categorized negligible. In line with the global translational symmetry of the WSe_2 crystals, the orientation of each layer is preserved by the screw dislocation. Hence, aligned spirals with all step edges in parallel were formed. Similar characteristics were recently reported for 2D materials.[53–55]

The terrace widths vary from 637 nm at smallest to 711 nm at largest for the crystal shown in Fig. 6(c) and (d). Consequently, the slope for each step varies in the range $0.0145 \leq s \leq 0.0180$. The average slope for the WSe_2 crystal is 0.0156 and is similar to the slope of 0.0126 reported by Chen et al.[56]

The majority of the features can be categorized into small steps and slopes as well as general low supersaturation condition per definition, see Fig. 7(a). Indeed, our data suggest that growth conditions are linked sufficiently accurate to low supersaturation. All examined height profiles indicate that WSe_2 was grown under conditions of low supersaturation.

Additional TRAGMIN modelling and CVT experiments performed in the predicted temperature range from 800 °C to 950 °C revealed comparable vapor pressure characteristics and thus similar growth. Indeed, WSe_2 crystals show step heights that correlate with smaller slopes at elevated temperatures. Differences in step heights and slopes should be linked to varying deposition temperatures and temperature gradients, whereas calculated transport rates are similar (915 °C → 860 °C: $\dot{m}_{calc.} = 1.63$ mg h^{-1} vs. 890 °C → 840 °C: $\dot{m}_{calc.} = 1.61$ mg h^{-1}). Crystals grown at 860 °C exhibit small slopes ($w < 400$ nm) and low step heights ($h < 5$ nm). Lower deposition temperatures indicate broader terrace widths ($w > 500$ nm) with height steps of around 10 nm. Crystals with a pyramid-like topography ($\vartheta_{sink} = 800$ °C) correlate with small steps and terrace widths, which results in narrowly arranged surface characteristics.

A semi-quantitative approach to further link theoretical considerations and the CVT experiments is to plot the difference of the respective equilibrium constant ΔK_p, i.e., $K_p(T_2) - K_p(T_1)$, for the dominant transport equilibrium eqn (1) from $T_2 \rightarrow T_1$, with $T_2 > T_1$, against the terrace width of the crystals.
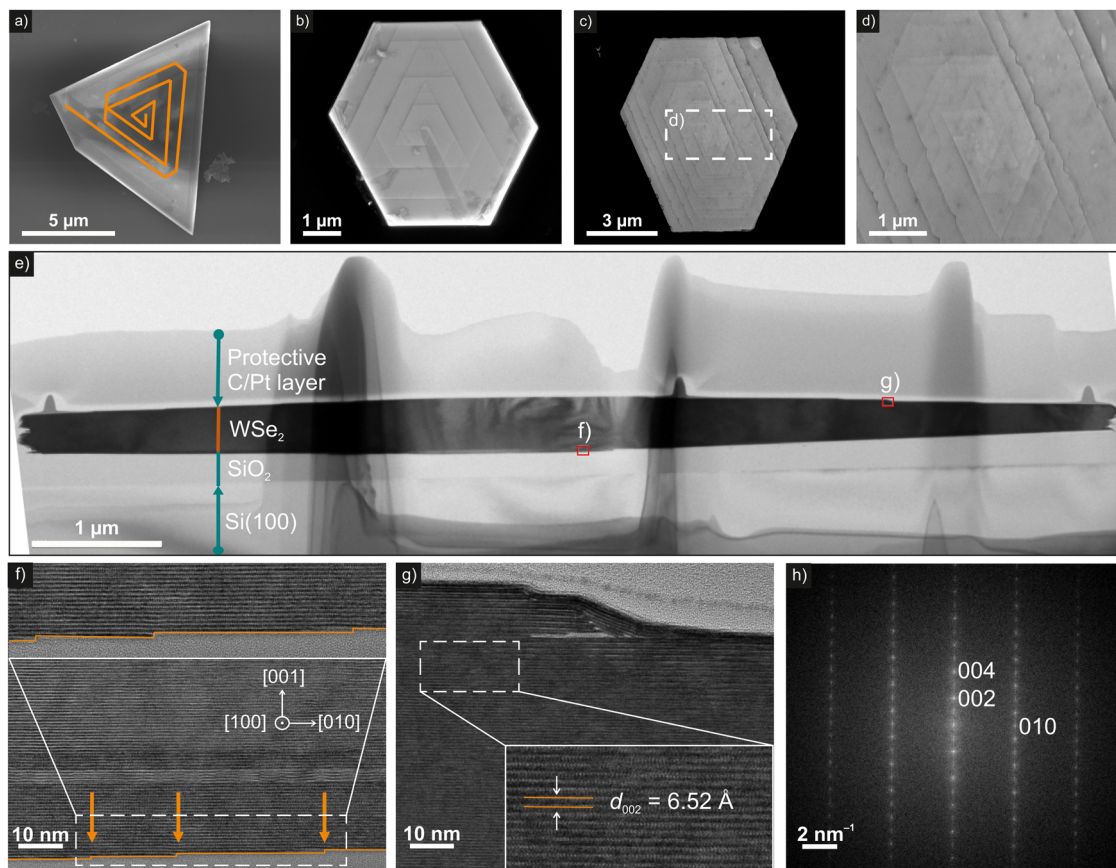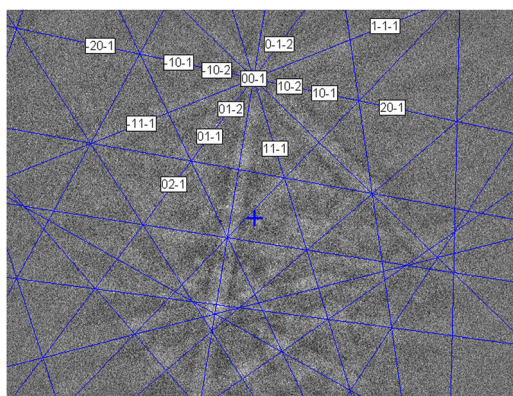
Fig. 4 Surface morphology and atomic structure analysis for as-grown WSe$_2$ with screw dislocations using SEM and TEM. (a)–(d) SEM images of triangular and hexagonal WSe$_2$ grown on an SiO$_2$@Si(100) substrate. Screw dislocation-driven growth is redrawn for the triangular crystal. (e) FIB cut of the hexagonally shaped WSe$_2$ crystal (c) with areas selected for high-resolution TEM highlighted. (f) and (g) Cross-sectional high-resolution TEM images of the back (f) and frontside (g) reveal individual steps of the fabricated FIB lamella of the crystals demonstrating a continuous 2H-phase over a larger area. Individual steps are highlighted in orange and depicted enlarged in the inset of (f). (h) Fourier transform (FT) of the area shown in (g).

Hereby, ΔK_p is a representative for the growth conditions chosen. The data for the average terrace width for each synthesis condition give a strong hint for a linear trend, see Fig. 7(b). Thereby, TRAGMIN simulations is a tool to predict a tightened temperature window for controlled growth of crystals with

Fig. 5 EBSD characterization for as-grown 2H-WSe$_2$ with screw dislocations with simulated Kikuchi lines and indexed zone axes.

screw dislocations and to fine-tune the characteristic features of the crystals.

Raman spectroscopy: confirmation of chirality. Alternation of interlayer interactions in layered materials by screw dislocations can change their electronic and vibrational properties. To address an effect of this factor, bulk-WSe$_2$ and the nm-scale WSe$_2$ samples with screw dislocations were investigated by Raman spectroscopy. Fig. 8 compares non-polarized spectra obtained with laser excitation at 532 nm (2.33 eV) and 660 nm (1.88 eV). The former is close to the energies of A$'$ and B excitons in bulk WSe$_2$ at ≈ 2.20 eV and induces resonance effects in the spectra,[57,58] while 660 nm is further away from energies of electronic excitations and is usually considered as non-resonant. We also used a 785 nm laser (1.58 eV), which matches the energy of the A exciton (1.59 eV),[59] but the spectra appeared similar to those excited at 660 nm and will not be discussed explicitly (ESI†).

When studied in back-scattering geometry with the laser beam perpendicular to the basal plane, WSe$_2$ in the D_{6h} factor group has only three first-order Raman-active vibrations at the Γ-point, one out-of-plane A$_{1g}$ and two in-plane 2 E$_{2g}$ modes. Experimental spectra of WSe$_2$ are usually dominated by nearly-
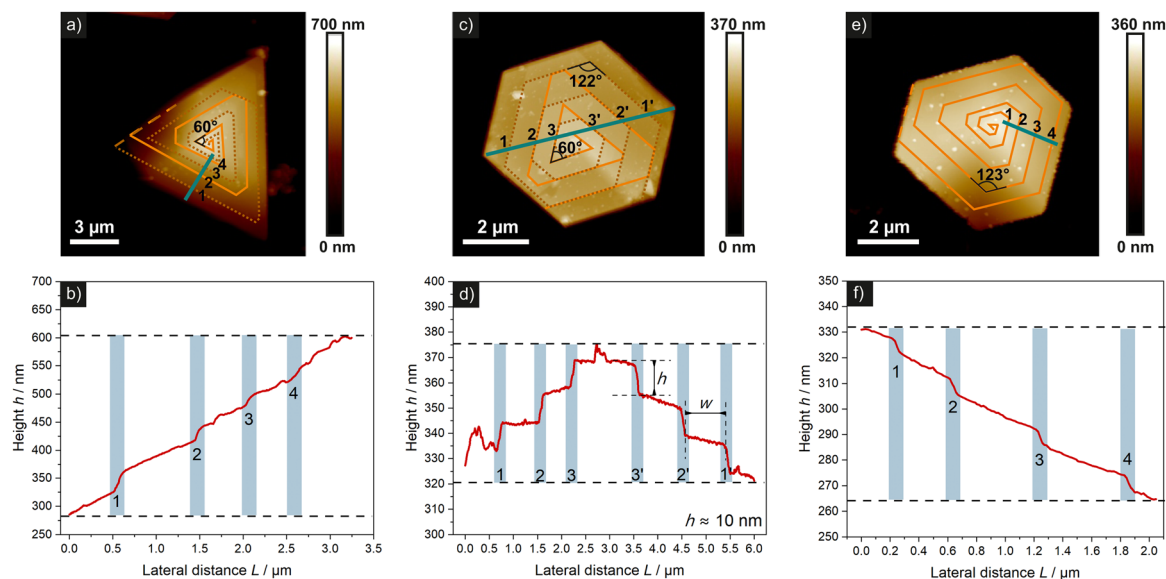
Fig. 6 AFM measurements of three representative nm-scale WSe$_2$ crystals with a right-handed spiral stacking topology. Depicted green measurement lines correspond to the respective height profiles below. For further characterization each height and terrace width were measured. Each step is indexed.
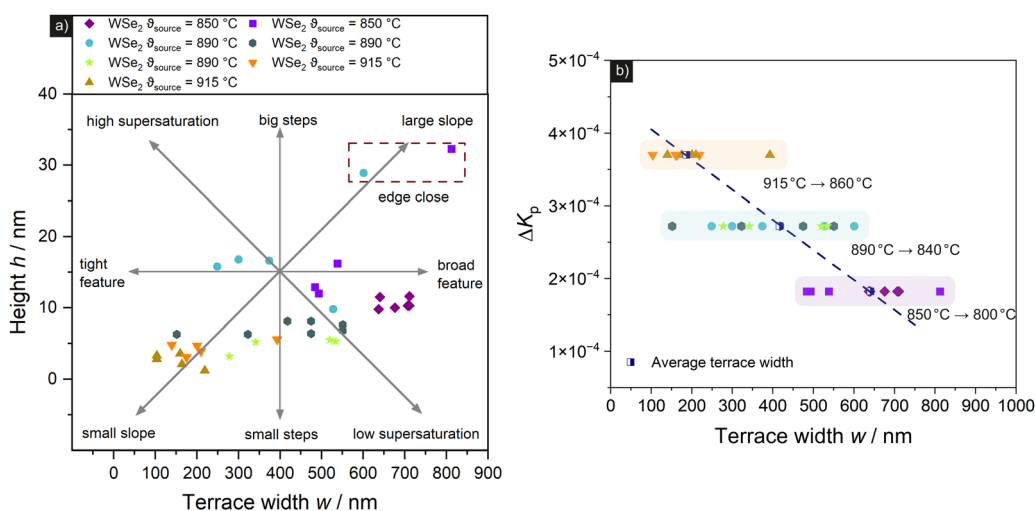

Fig. 7 (a) Surface morphology characteristics of several WSe$_2$ crystals with screw dislocations. All heights and terrace widths were determined by AFM height profiles. Grey arrows indicate general growth conditions and related crystal features. Features marked by the dashed rectangle represent edge-close steps on the crystal. (b) Dependency of average terrace width from calculated temperature-dependent equilibrium constant K_p for each synthesis temperature regime.

degenerate E_{2g}^1 and A_{1g} peaks at 247 cm^{-1} and 250 cm^{-1}, accompanied by a broader band at ≈ 260 cm^{-1} associated with the two-phonon 2 LA(M) feature. In fact, the latter band has an asymmetric shape with 2–3 unresolved components, whose assignment is not completely clear yet. For instance, in ref. 60, the feature at 256 cm^{-1} was ascribed to the B$_{2g}$(M) mode, while the 2 LA(M) proper identified at 260 cm^{-1}, an assignment for the shoulder at 263 cm^{-1} to A(M) mode as was proposed in ref. 57. As the 220–280 cm^{-1} range has the highest Raman activity and narrow spacing of the peaks, we plot it enlarged in insets of Fig. 8. Aside from the first-order phonons, Raman spectra of WSe$_2$ are rich with a number of second-order

features, whose relative intensity depends on the excitation wavelength and is stronger for the resonant excitation at 532 nm. A tentative assignment for prominent second-order peaks and formally inactive modes is given in Fig. 8(a) and supplement based on the data from ref. 57 and 60–64.

All Raman modes detected for the bulk-WSe$_2$ reference were also ascribed for the nm-scale crystals. Second-order features are observed for the latter with similar relative intensities and, within accuracy limits of 0.1–0.2 cm^{-1}, at the same peak positions as for the bulk WSe$_2$. However, there are also certain differences between the spectra, particularly visible in the 220–280 cm^{-1} range encompassing E$_{2g}^1$, A$_{1g}$, and 2 LA(M) modes.
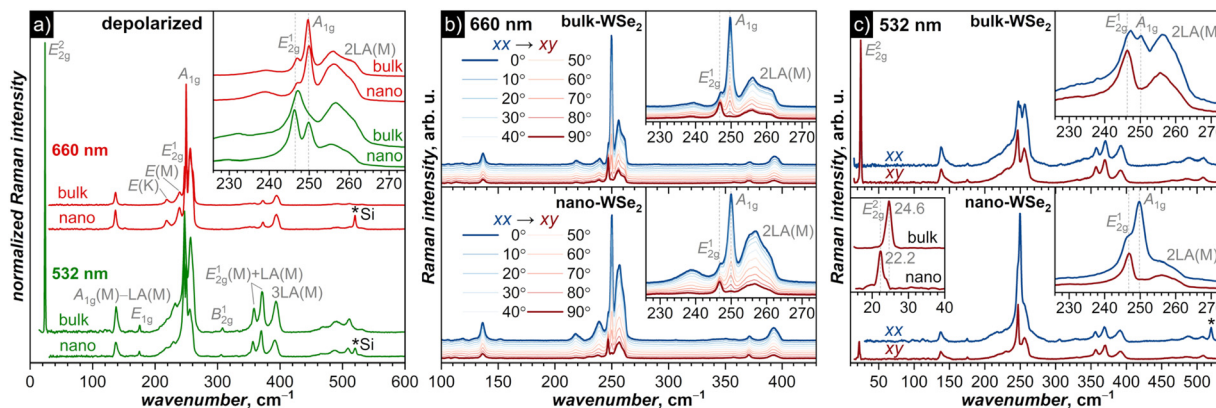
Fig. 8 (a) Raman spectra of pre-synthesized bulk-WSe$_2$, and nm-scale WSe$_2$ crystals excited with depolarized lasers at 660 nm and 532 nm. (b) Polarized spectra of bulk and nano-WSe$_2$ excited at 660 nm and measured with step-wise rotation of the laser polarization plane with respect to the crystal and polarization direction of the detector (angles of 0° and 90° correspond to xx and xy polarization geometries). (c) Polarized spectra of bulk and nano-WSe$_2$ excited at 532 nm with two polarization geometries, parallel (xx) and cross-polarized (xy). In each panel, insets show the range of 226 cm^{-1} ≤ $\tilde{v}$ ≤ 274 cm^{-1}, depicted enlarged for better comparison of the most prominent features. Additional inset in (c) compares the range of low-frequency shear mode (E_{2g}^2) of bulk and nano-WSe$_2$ measured in the cross-polarized geometry.

Under the 660 nm excitation, A_{1g} has considerably higher intensity than E_{2g}^1 both in bulk and nm-scale crystals. The main difference between the samples is in the 2 LA(M) band, which in the bulk-WSe$_2$ has lower relative intensity but a better-defined shape with two features at 256 cm^{-1} and 261 cm^{-1}. In the nano-WSe$_2$, the 2 LA(M) band has higher intensity, but the peak shape is more asymmetric and encompasses at least three unresolved features at 255, 256, and 261 cm^{-1}. Under the 532 nm excitation, the intensity ratio of the E_{2g}^1/A_{1g} peak changes considerably when compared to that of the spectra obtained with the 660 nm laser. In the bulk-WSe$_2$, only the E_{2g}^1 peak is clearly visible, while A_{1g} is much weaker than E_{2g}^1 and the 2 LA(M) bands and cannot be resolved. The nano-WSe$_2$ exhibits quite a different pattern in that A_{1g} is only slightly weaker than E_{2g}^1 and is clearly visible, while intensity of the 2 LA(M) band is reduced considerably relative to the E_{2g}^1/A_{1g} pair.

To confirm symmetry assignments and to find if crystals with screw dislocations have different angular dependence of polarization, we performed polarized Raman measurements. Fig. 8(b) shows the spectra of bulk and nano-WSe$_2$ obtained by rotation of the 660 nm laser polarization in 10° steps, from the parallel orientation of the laser and analyzer (0°, xx) to the cross-polarized geometry (90°, xy). For D_{6h} symmetry and propagation of incident and scattered light along the z-axis, A_{1g} modes are active in xx and forbidden in xy orientations, while intensity of E_{2g} mode should not depend on the angle. In accordance with symmetry, we do observe a strong modulation of the A_{1g} peak from the full-scale at 0° to zero at 90°, whereas the E_{2g} peak remains nearly constant. The angular dependence is identical for bulk and nano-WSe$_2$, showing that the screw dislocation does not affect the local symmetry. Similarly, xx and xy-polarized measurements with the 532 nm excitation confirmed assignments of A_{1g} and E_{2g} modes and their regular polarization dependence (Fig. 8(c)). For the bulk sample, a weak signal of the A_{1g} mode became visible in the xx polarization, while enhanced intensity of the A_{1g} mode in the nano-WSe$_2$ is further corroborated in the xx-polarized spectrum.

Low-frequency interlayer modes can be particularly interesting for the analysis of the morphological aspects in 2D materials as they are sensitive to the interlayer stacking geometry and interactions. While interlayer breathing mode of bulk-WSe$_2$ has B_{2g}^2 symmetry and is optically silent, the shear mode with E_{2g}^2 symmetry, in which layers are displaced in the antiparallel direction, is Raman active and occurs near 25 cm^{-1}.[61]

Although the low intensity and overlap with the strong Rayleigh background of the laser precluded detection of the E_{2g}^2 mode under 660 nm excitation, a sharp and very strong peak at 24.6 cm^{-1} was observed for the bulk sample excited with the 532 nm laser (Fig. 8(a)). The peak has similar intensity in xx and xy polarization geometries, confirming its assignment to the E_{2g}^2 symmetry. For the nano-WSe$_2$ sample, we could not reliably detect the shear mode in non-polarized or xx-polarized spectra because of the strong laser tail, but suppression of the Rayleigh background in the xy polarization allowed a detection of the weaker signal at 22.2 cm^{-1} (Fig. 8(c)). The E_{2g}^2 mode intensity in nano-WSe$_2$ is three times smaller than the intensity of the E_{2g}^1 mode, while in the bulk-WSe$_2$ the shear mode is stronger than E_{2g}^1 by a factor of 2.5. The frequency shift of 2.4 cm^{-1} between the bulk and nano-WSe$_2$ is also quite characteristic and is in line with the earlier report by Shearer $et\ al.$,[48] who found that the crystals with a hexagonal spiral dislocation had the shear mode at the same frequency as in bulk-WSe$_2$, and crystals with a triangular dislocation did not show a shear mode at all, while mixed hexagonal-triangular crystals exhibited a downshift by 3 cm^{-1}.

Chirality of the crystals with screw dislocations suggests that they should show an optical activity,[65–67] which we addressed by circularly polarized (CP) Raman spectroscopy.[68] According to the selection rules for CP-Raman, A_{1g} mode of WSe$_2$ is active when both incident and scattered lights have the same helicity ($\sigma^+\sigma^+$ and $\sigma^-\sigma^-$ configurations), whereas the E_{2g} mode is active for opposite polarizations of the incident and scattered lights ($\sigma^+\sigma^-$ and $\sigma^-\sigma^+$ configurations).[69] Indeed, CP-Raman spectra
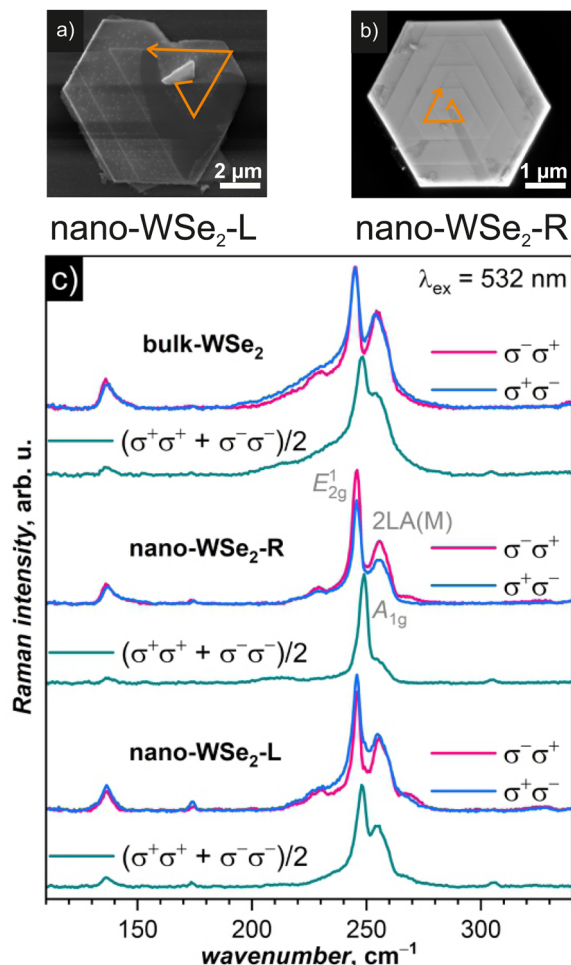
Fig. 9 (a) and (b) SEM images of WSe$_2$ crystals with screw dislocations and opposite chiralities: (a) left-handed, nano-WSe$_2$-L, (b) right-handed, nano-WSe$_2$-R. (c) Circular-polarized Raman spectra of bulk-WSe$_2$ and crystals with screw dislocations, whose SEM images are shown in (a) and (b). Spectra were excited with a 532 nm laser.

of bulk and nano-WSe$_2$ samples demonstrate mutually exclusive activity of E$_{2g}^1$ and A$_{1g}$ modes (Fig. 9). For the achiral bulk-WSe$_2$, E$_{2g}^1$ mode has the same intensity in the $\sigma^+\sigma^-$ and $\sigma^-\sigma^+$ spectra. However, in the crystals with screw dislocations (Fig. 9a and b), $\sigma^+\sigma^-$ and $\sigma^-\sigma^+$ intensities of the E$_{2g}^1$ peak are noticeably different. The $\sigma^+\sigma^-$ intensity exceeds the $\sigma^-\sigma^+$ intensity in the right-handed crystal by 29%, whereas in the left-handed crystal the $\sigma^-\sigma^+$ peak is higher than the $\sigma^+\sigma^-$ peak by 15%. The less pronounced Raman optical activity of the left-handed crystal is presumably caused by the larger size of the terraces. Interestingly, the vast majority of synthesized nano-crystals appeared to be right-handed, whereas left-handed crystals were only observed from 915 °C → 860 °C. We studied one of the crystals in different places and did not find a considerable variation of the polarization (ESI†). Based on the identical substrate preparation but different deposition temperatures for right and left-handed spirals, we assume the sink temperature to be the main factor to affect the growth, and thus the temperature ranges can serve as selectivity criteria to differentiate between the two types of WSe$_2$ spirals by CVT.

To summarize, while demonstrating a similarity in the overall vibrational pattern, Raman measurements also revealed clear distinctions between bulk-WSe$_2$ and nano-WSe$_2$ crystals with screw dislocations. The most pronounced differences are in the intensity and frequency of the interlayer shear mode, and in the relative intensities of E$_{2g}^1$, A$_{1g}$, and 2 LA(M) modes. While the former points to the changes in the interlayer interactions, the latter highlights the alterations in the Raman resonance conditions and can therefore evidence the variation in the electronic structure of WSe$_2$.

Conclusion

In summary, triangular and hexagonal pyramid-like WSe$_2$ nano-scale crystals with screw dislocations were synthesized by custom-designed CVT experiments based on a rational synthesis approach applying thermodynamic modelling. The simulations allowed designing a temperature range for optimized growth conditions during the CVT process. Vibrational spectroscopy using Raman revealed all modes detected for bulk and nano-WSe$_2$ were found with similar peak intensities and positions with main differences including both the intensity ratio of the E$_{2g}^1$/A$_{1g}$ peak changed significantly and the 2 LA(M) band characterized with a more asymmetric shape for nano-WSe$_2$. The screw dislocation was found to have no effect on the local symmetry according to the angular dependence. Right and left-handed spiral stackings affected the intensity of the E$_{2g}^1$ mode by 29% and 15%, respectively. With EBSD, we were able to elucidate the high crystallinity of the as-grown WSe$_2$ directly on the substrate, index Kikuchi lines and link it to the 2H modification. The EBSD patterns indicate a gradual orientation change across the sample which corresponds to a convex curvature. We determined the horizontal and vertical pattern shifts and calculated the respective curvature radii, with the curvature radius along the horizontal orientation found to be significantly larger. Key features of the screw dislocation were found to be a step height of around 10 nm with the respective terrace widths varying depending on the modelled temperature ranges. In addition, characteristics are linked to theoretical considerations. Thereby, the terrace widths correlate linearly with the supersaturation conditions during the crystal growth, which is represented by the temperature-dependent equilibrium constant. Connecting thermodynamic considerations with actual CVT experiments enabled determining the optimum reaction conditions for the low supersaturation and thus opens up a pathway for further rational design of screw dislocation-driven growth by CVT.

Author contributions

P. S., S. H. and B. B. conceived and designed the project. P. P. conducted the synthesis of materials, thermodynamic modelling and analysis, optical microscopy/SEM, AFM and pXRD characterization and analysis. D. W. performed the HR-TEM measurements. A. A. P. contributed to the Raman analysis. J. G.

and T. R. carried out the EBSD measurements. P. C. and T. R. carried out the EBSD analysis. The manuscript was written by P. P. based on contributions from all authors. S. H. and B. B. were responsible for the project management.

Data availability

The data supporting this article have been included in the ESI.†

Conflicts of interest

There are no conflicts to declare.

Acknowledgements

References

1 K. S. Novoselov, A. K. Geim, S. V. Morozov, D. Jiang, Y. Zhang, S. V. Dubonos, I. V. Grigorieva and A. A. Firsov, Electric Field Effect in Atomically Thin Carbon Films, *Science*, 2004, **306**(5696), 666–669, DOI: **10.1126/science.1102896**.

2 K. S. Novoselov, A. Mishchenko, A. Carvalho and A. H. Castro Neto, 2D Materials and van der Waals Heterostructures, *Science*, 2016, **353**(6298), aac9439, DOI: **10.1126/science.aac9439**.

3 Y. Liu, Y. Huang and X. Duan, van der Waals Integration before and beyond Two-Dimensional Materials, *Nature*, 2019, **567**(7748), 323–333, DOI: **10.1038/s41586-019-1013-x**.

4 S. J. McDonnell and R. M. Wallace, Atomically-Thin Layered Films for Device Applications Based upon 2D TMDC Materials, *Thin Solid Films*, 2016, **616**, 482–501, DOI: **10.1016/j.tsf.2016.08.068**.

5 H. Zhang, L.-M. Liu and W.-M. Lau, Dimension-Dependent Phase Transition and Magnetic Properties of VS$_2$, *J. Mater. Chem. A*, 2013, **1**(36), 10821–10828, DOI: **10.1039/C3TA12098H**.

6 G. Fiori, F. Bonaccorso, G. Iannaccone, T. Palacios, D. Neumaier, A. Seabaugh, S. K. Banerjee and L. Colombo, Electronics Based on Two-Dimensional Materials, *Nat. Nanotechnol.*, 2014, **9**(10), 768–779, DOI: **10.1038/nnano.2014.207**.

7 F. H. L. Koppens, T. Mueller, P. Avouris, A. C. Ferrari, M. S. Vitiello and M. Polini, Photodetectors Based on Graphene, Other Two-Dimensional Materials and Hybrid Systems, *Nat. Nanotechnol.*, 2014, **9**(10), 780–793, DOI: **10.1038/nnano.2014.215**.

8 W.-X. Zhou and K.-Q. Chen, First-Principles Determination of Ultralow Thermal Conductivity of Monolayer WSe$_2$, *Sci. Rep.*, 2015, **5**(1), 15070, DOI: **10.1038/srep15070**.

9 N. Kumari, M. Kalyan, S. Ghosh, A. R. Maity and R. Mukherjee, Possible Negative Correlation between Electrical and Thermal Conductivity in P-Doped WSe$_2$ Single Crystal, *Mater. Res. Express*, 2021, **8**(4), 045902, DOI: **10.1088/2053-1591/abf682**.

10 K. K. Kam and B. A. Parkinson, Detailed Photocurrent Spectroscopy of the Semiconducting Group VIB Transition Metal Dichalcogenides, *J. Phys. Chem.*, 1982, **86**(4), 463–467, DOI: **10.1021/j100393a010**.

11 S. A. Han, R. Bhatia and S.-W. Kim, Synthesis, Properties and Potential Applications of Two-Dimensional Transition Metal Dichalcogenides, *Nano Converge.*, 2015, **2**(1), 1–14, DOI: **10.1186/s40580-015-0048-4**.

12 R. Murray and B. Evans, The Thermal Expansion of 2H-MoS2 and 2H-WSe$_2$ between 10 and 320 K, *J. Appl. Crystallogr.*, 1979, **12**(3), 312–315, DOI: **10.1107/S0021889879012528**.

13 Y. J. Park, H.-S. So, H. Hwang, D. S. Jeong, H. J. Lee, J. Lim, C. G. Kim and H. S. Shin, Synthesis of 1T WSe$_2$ on an Oxygen-Containing Substrate Using a Single Precursor, *ACS Nano*, 2022, **16**(7), 11059–11065, DOI: **10.1021/acsnano.2c03762**.

14 E. Y. Andrei, D. K. Efetov, P. Jarillo-Herrero, A. H. MacDonald, K. F. Mak, T. Senthil, E. Tutuc, A. Yazdani and A. F. Young, The Marvels of Moiré Materials, *Nat. Rev. Mater.*, 2021, **6**(3), 201–206, DOI: **10.1038/s41578-021-00284-1**.

15 Y. Cao, V. Fatemi, S. Fang, K. Watanabe, T. Taniguchi, E. Kaxiras and P. Jarillo-Herrero, Unconventional Superconductivity in Magic-Angle Graphene Superlattices, *Nature*, 2018, **556**(7699), 43–50, DOI: **10.1038/nature26160**.

16 G. Chen, L. Jiang, S. Wu, B. Lyu, H. Li, B. L. Chittari, K. Watanabe, T. Taniguchi, Z. Shi, J. Jung, Y. Zhang and F. Wang, Evidence of a Gate-Tunable Mott Insulator in a Trilayer Graphene Moiré Superlattice, *Nat. Phys.*, 2019, **15**(3), 237–241, DOI: **10.1038/s41567-018-0387-2**.

17 K. L. Seyler, P. Rivera, H. Yu, N. P. Wilson, E. L. Ray, D. G. Mandrus, J. Yan, W. Yao and X. Xu, Signatures of Moiré-Trapped Valley Excitons in MoSe$_2$/WSe$_2$ Heterobilayers, *Nature*, 2019, **567**(7746), 66–70, DOI: **10.1038/s41586-019-0957-1**.

18 K. Tran, G. Moody, F. Wu, X. Lu, J. Choi, K. Kim, A. Rai, D. A. Sanchez, J. Quan and A. Singh, Evidence for Moiré Excitons in van der Waals Heterostructures, *Nature*, 2019, **567**(7746), 71–75, DOI: **10.1038/s41586-019-0975-z**.

19 Q. Xu, Y. Guo and L. Xian, Moiré Flat Bands in Twisted 2D Hexagonal VdW Materials, *2D Mater.*, 2021, **9**(1), 14005, DOI: **10.1088/2053-1583/ac3a98**.

20 S. A. Morin, M. J. Bierman, J. Tong and S. Jin, Mechanism and Kinetics of Spontaneous Nanotube Growth Driven by Screw Dislocations, *Science*, 2010, **328**(5977), 476–480, DOI: **10.1126/science.1182977**.

21 Y. Sun, Y. Jiang, J. Jiang, T. Li and M. Liu, Keto-Form Directed Hierarchical Chiral Self-Assembly of Schiff Base Derivatives with Amplified Circularly Polarized Luminescence, *Chin. Chem. Lett.*, 2024, **35**(1), 108409, DOI: **10.1016/j.cclet.2023.108409**.

22 J. Yeom, B. Yeom, H. Chan, K. W. Smith, S. Dominguez-Medina, J. H. Bahng, G. Zhao, W.-S. Chang, S.-J. Chang,

A. Chuvilin, D. Melnikau, A. L. Rogach, P. Zhang, S. Link, P. Král and N. A. Kotov, Chiral Templating of Self-Assembling Nanostructures by Circularly Polarized Light, *Nat. Mater.*, 2015, **14**(1), 66–72, DOI: **10.1038/nmat4125**.

23 T. D. James, K. R. A. Samankumara Sandanayake and S. Shinkai, Chiral Discrimination of Monosaccharides Using a Fluorescent Molecular Sensor, *Nature*, 1995, **374**(6520), 345–347, DOI: **10.1038/374345a0**.

24 M. Bartók, Unexpected Inversions in Asymmetric Reactions: Reactions with Chiral Metal Complexes, Chiral Organocatalysts, and Heterogeneous Chiral Catalysts, *Chem. Rev.*, 2010, **110**(3), 1663–1705, DOI: **10.1021/cr9002352**.

25 R. Naaman and D. H. Waldeck, Spintronics and Chirality: Spin Selectivity in Electron Transport Through Chiral Molecules, *Annu. Rev. Phys. Chem.*, 2015, **66**(1), 263–281, DOI: **10.1146/annurev-physchem-040214-121554**.

26 R. Tanuma, I. Kamata, J. P. Hadorn and H. Tsuchida, Two-Photon-Excited, Three-Dimensional Photoluminescence Imaging and Dislocation-Line Analysis of Threading Dislocations in 4H-SiC, *J. Appl. Phys.*, 2018, **124**(12), 125703, DOI: **10.1063/1.5043238**.

27 D.-B. Zhang, T. Dumitrică and G. Seifert, Helical Nanotube Structures of $MoSe_2$ with Intrinsic Twisting: An Objective Molecular Dynamics Study, *Phys. Rev. Lett.*, 2010, **104**(6), 065502, DOI: **10.1103/PhysRevLett.104.065502**.

28 J. Ai, Y. Wang, L. Li, J. Wang, T. Bai, S. Che and L. Han, Determination of Multilevel Chirality in Nickel Molybdate Films by Electron Crystallography, *Nano Res.*, 2024, **17**(9), 8571–8577, DOI: **10.1007/s12274-024-6865-1**.

29 B. Sung, A. de la Cotte and E. Grelet, Chirality-Controlled Crystallization via Screw Dislocations, *Nat. Commun.*, 2018, **9**(1), 1405, DOI: **10.1038/s41467-018-03745-4**.

30 T. Verbiest, S. Van Elshocht, M. Kauranen, L. Hellemans, J. Snauwaert, C. Nuckolls, T. J. Katz and A. Persoons, Strong Enhancement of Nonlinear Optical Properties Through Supramolecular Chirality, *Science*, 1998, **282**(5390), 913–915, DOI: **10.1126/science.282.5390.913**.

31 R. Naaman, Y. Paltiel and D. H. Waldeck, Chiral Molecules and the Electron Spin, *Nat. Rev. Chem.*, 2019, **3**(4), 250–260, DOI: **10.1038/s41570-019-0087-1**.

32 G. Chang, B. J. Wieder, F. Schindler, D. S. Sanchez, I. Belopolski, S.-M. Huang, B. Singh, D. Wu, T.-R. Chang, T. Neupert, S.-Y. Xu, H. Lin and M. Z. Hasan, Topological Quantum Properties of Chiral Crystals, *Nat. Mater.*, 2018, **17**(11), 978–985, DOI: **10.1038/s41563-018-0169-3**.

33 J. B. Legma, G. Vacquier and A. Casalot, Chemical Vapour Transport of Molybdenum and Tungsten Diselenides by Various Transport Agents, *J. Cryst. Growth*, 1993, **130**(1–2), 253–258, DOI: **10.1016/0022-0248(93)90859-U**.

34 A. A. Al-Hilli and B. L. Evans, The Preparation and Properties of Transition Metal Dichalcogenide Single Crystals, *J. Cryst. Growth*, 1972, **15**(2), 93–101, DOI: **10.1016/0022-0248(72)90129-7**.

35 R. Kershaw, M. Vlasse and A. Wold, The Preparation of and Electrical Properties of Niobium Selenide and Tungsten Selenide, *Inorg. Chem.*, 1967, **6**(8), 1599–1602, DOI: **10.1021/ic50054a043**.

36 M. Bougouma, B. Nisol, T. Doneux, B. Guel, T. Segato, F. Reniers, M.-P. Delplancke-Ogletree, J. B. Legma and C. Buess-Herman, Growth and Characterization of WSe_2 Single Crystals Using $TeCl_4$ as Transport Agent, *J. Cryst. Growth*, 2016, **453**, 111–118, DOI: **10.1016/j.jcrysgro.2016.08.025**.

37 N. D. Boscher, C. J. Carmalt and I. P. Parkin, Atmospheric Pressure Chemical Vapor Deposition of WSe_2 Thin Films on Glass—Highly Hydrophobic Sticky Surfaces, *J. Mater. Chem.*, 2006, **16**(1), 122–127, DOI: **10.1039/B514440J**.

38 L. Chen, B. Liu, A. N. Abbas, Y. Ma, X. Fang, Y. Liu and C. Zhou, Screw-Dislocation-Driven Growth of Two-Dimensional Few-Layer and Pyramid-like WSe_2 by Sulfur-Assisted Chemical Vapor Deposition, *ACS Nano*, 2014, **8**(11), 11543–11551, DOI: **10.1021/nn504775f**.

39 X. Wang, Y. Li, L. Zhuo, J. Zheng, X. Peng, Z. Jiao, X. Xiong, J. Han and W. Xiao, Controllable Growth of Two-Dimensional WSe_2 Using Salt as Co-Solvent, *CrystEngComm*, 2018, **20**(40), 6267–6272, DOI: **10.1039/C8CE01162A**.

40 F. Hansen, M. Wels, S. Froeschke, A. Popov, D. Wolf, B. Büchner, P. Schmidt and S. Hampel, Thermodynamic Evaluation and Chemical Vapor Transport of Few-Layer WTe_2, *Cryst. Growth Des.*, 2020, **20**(11), 7341–7349, DOI: **10.1021/acs.cgd.0c01004**.

41 G. Krabbes, W. Bieger, K.-H. Sommer, T. Söhnel and U. Steiner, *GMIN Version 5.2: Package TRAGMIN for Calculation of Thermodynamic Equilibrium*, Dresden, 2014, **https://www.htw-dresden.de/luc/forschung/chemieingenieurwesen/festkoerperchemie/tragmin**.

42 W. J. Schutte, J. L. De Boer and F. Jellinek, Crystal Structures of Tungsten Disulfide and Diselenide, *J. Solid State Chem.*, 1987, **70**(2), 207–209, DOI: **10.1016/0022-4596(87)90057-0**.

43 Y. Zhao and S. Jin, Stacking and Twisting of Layered Materials Enabled by Screw Dislocations and Non-Euclidean Surfaces, *Acc. Mater. Res.*, 2022, **3**(3), 369–378, DOI: **10.1021/accountsmr.1c00245**.

44 Y. Zhao, C. Zhang, D. D. Kohler, J. M. Scheeler, J. C. Wright, P. M. Voyles and S. Jin, Supertwisted Spirals of Layered Materials Enabled by Growth on Non-Euclidean Surfaces, *Science*, 2020, **370**(6515), 442–445, DOI: **10.1126/science.abc4284**.

45 P. Haasen, *Physikalische Metallkunde*, Springer, Berlin, 3rd edn, 2013, p. 255.

46 S. A. Morin, A. Forticaux, M. J. Bierman and S. Jin, Screw Dislocation-Driven Growth of Two-Dimensional Nanoplates, *Nano Lett.*, 2011, **11**(10), 4449–4455, DOI: **10.1021/nl202689m**.

47 A. Zhuang, J. Li, Y. Wang, X. Wen, Y. Lin, B. Xiang, X. Wang and J. Zeng, Screw-Dislocation-Driven Bidirectional Spiral Growth of Bi_2Se_3 Nanoplates, *Angew. Chem., Int. Ed.*, 2014, **53**(25), 6425–6429, DOI: **10.1002/anie.201403530**.

48 M. J. Shearer, L. Samad, Y. Zhang, Y. Zhao, A. Puretzky, K. W. Eliceiri, J. C. Wright, R. J. Hamers and S. Jin, Complex and Noncentrosymmetric Stacking of Layered Metal Dichalcogenide Materials Created by Screw Dislocations, *J. Am. Chem. Soc.*, 2017, **139**(9), 3496–3504, DOI: **10.1021/jacs.6b12559**.

49 M. C. C. Giacovazzo, H. L. Monaco, G. Artioli, D. Viterbo, G. Ferraris, G. Gilli and G. Zanotti, *Fundamentals of Crystallography*, Oxford University Press, Oxford, 2nd edn, 2002.

50 J. Dong, L. Zhang and F. Ding, Kinetics of Graphene and 2D Materials Growth, *Adv. Mater.*, 2019, **31**(9), 1801583, DOI: **10.1002/adma.201801583**.

51 M. J. Greenberg, *Euclidean and Non-Euclidean Geometries: Development and History*, W.H. Freeman and Company, New York, 4th edn, 2007.

52 M. J. Bierman, Y. K. A. Lau, A. V. Kvit, A. L. Schmitt and S. Jin, Dislocation-Driven Nanowire Growth and Eshelby Twist, *Science*, 2008, **320**(5879), 1060–1063, DOI: **10.1126/science.1157131**.

53 T. Tong, R. Chen, Y. Ke, Q. Wang, X. Wang, Q. Sun, J. Chen, Z. Gu, Y. Yu, H. Wei, Y. Hao, X. Fan and Q. Zhang, Giant Second Harmonic Generation in Supertwisted WS$_2$ Spirals Grown in Step-Edge Particle-Induced Non-Euclidean Surfaces, *ACS Nano*, 2024, **18**(33), 21939–21947, DOI: **10.1021/acsnano.4c02807**.

54 R. Y. Tay, H. J. Park, J. Lin, Z. K. Ng, L. Jing, H. Li, M. Zhu, S. H. Tsang, Z. Lee and E. H. T. Teo, Concentric and Spiral Few-Layer Graphene: Growth Driven by Interfacial Nucleation *vs.* Screw Dislocation, *Chem. Mater.*, 2018, **30**(19), 6858–6866, DOI: **10.1021/acs.chemmater.8b03024**.

55 H. J. Park, R. Y. Tay, X. Wang, W. Zhao, J. H. Kim, R. S. Ruoff, F. Ding, E. H. T. Teo and Z. Lee, Double-Spiral Hexagonal Boron Nitride and Shear Strained Coalescence Boundary, *Nano Lett.*, 2019, **19**(7), 4229–4236, DOI: **10.1021/acs.nanolett.8b05034**.

56 L. Chen, B. Liu, A. N. Abbas, Y. Ma, X. Fang, Y. Liu and C. Zhou, Screw-Dislocation-Driven Growth of Two-Dimensional Few-Layer and Pyramid-like WSe$_2$ by Sulfur-Assisted Chemical Vapor Deposition, *ACS Nano*, 2014, **8**(11), 11543–11551, DOI: **10.1021/nn504775f**.

57 E. Del Corro, H. Terrones, A. Elias, C. Fantini, S. Feng, M. A. Nguyen, T. E. Mallouk, M. Terrones and M. A. Pimenta, Excited Excitonic States in 1L, 2L, 3L, and Bulk WSe$_2$ Observed by Resonant Raman Spectroscopy, *ACS Nano*, 2014, **8**(9), 9629–9635, DOI: **10.1021/nn504088g**.

58 A. R. Beal, J. C. Knights and W. Y. Liang, Transmission Spectra of Some Transition Metal Dichalcogenides. II. Group VIA: Trigonal Prismatic Coordination, *J. Phys. C: Solid State Phys.*, 1972, **5**(24), 3540–3551, DOI: **10.1088/0022-3719/5/24/016**.

59 R. F. Frindt, The Optical Properties of Single Crystals of WSe$_2$ and MoTe$_2$, *J. Phys. Chem. Solids*, 1963, **24**(9), 1107–1108, DOI: **10.1016/0022-3697(63)90024-6**.

60 L. Du, M. Liao, J. Tang, Q. Zhang, H. Yu, R. Yang, K. Watanabe, T. Taniguchi, D. Shi, Q. Zhang and G. Zhang, Strongly Enhanced Exciton-Phonon Coupling in Two-Dimensional WSe$_2$, *Phys. Rev. B*, 2018, **97**(23), 235145, DOI: **10.1103/PhysRevB.97.235145**.

61 D. G. Mead and J. C. Irwin, Long Wavelength Optic Phonons in WSe$_2$, *Can. J. Phys.*, 1977, **55**(5), 379–382, DOI: **10.1139/p77-052**.

62 X. Luo, Y. Zhao, J. Zhang, M. Toh, C. Kloc, Q. Xiong and S. Y. Quek, Effects of Lower Symmetry and Dimensionality on Raman Spectra in Two-Dimensional WSe$_2$, *Phys. Rev. B: Condens. Matter Mater. Phys.*, 2013, **88**(19), 195313, DOI: **10.1103/PhysRevB.88.195313**.

63 K. Akintola, G. T. Andrews, S. H. Curnoe, M. R. Koehler and V. Keppens, Raman and Brillouin Scattering Studies of Bulk 2H-WSe$_2$, *J. Phys.: Condens. Matter*, 2015, **27**(39), 395401, DOI: **10.1088/0953-8984/27/39/395401**.

64 X. Zhang, Q.-H. Tan, J.-B. Wu, W. Shi and P.-H. Tan, Review on the Raman Spectroscopy of Different Types of Layered Materials, *Nanoscale*, 2016, **8**(12), 6435–6450, DOI: **10.1039/C5NR07205K**.

65 L. Zhang, K. Liu, A. B. Wong, J. Kim, X. Hong, C. Liu, T. Cao, S. G. Louie, F. Wang and P. Yang, Three-Dimensional Spirals of Atomic Layered MoS$_2$, *Nano Lett.*, 2014, **14**(11), 6418–6423, DOI: **10.1021/nl502961e**.

66 X. Fan, Y. Jiang, X. Zhuang, H. Liu, T. Xu, W. Zheng, P. Fan, H. Li, X. Wu, X. Zhu, Q. Zhang, H. Zhou, W. Hu, X. Wang, L. Sun, X. Duan and A. Pan, Broken Symmetry Induced Strong Nonlinear Optical Effects in Spiral WS$_2$ Nanosheets, *ACS Nano*, 2017, **11**(5), 4892–4898, DOI: **10.1021/acsnano.7b01457**.

67 P. K. Barman, P. V. Sarma, M. M. Shaijumon and R. N. Kini, High Degree of Circular Polarization in WS$_2$ Spiral Nanostructures Induced by Broken Symmetry, *Sci. Rep.*, 2019, **9**(1), 2784, DOI: **10.1038/s41598-019-39246-7**.

68 Y. Zhao, B. Xu, L. Tong and J. Zhang, The Helicity of Raman Scattered Light: Principles and Applications in Two-Dimensional Materials, *Sci. China: Chem.*, 2022, **65**(2), 269–283, DOI: **10.1007/s11426-021-1119-4**.

69 S. Kim, K. Kim, J.-U. Lee and H. Cheong, Excitonic Resonance Effects and Davydov Splitting in Circularly Polarized Raman Spectra of Few-Layer WSe$_2$, *2D Mater.*, 2017, **4**(4), 045002, DOI: **10.1088/2053-1583/aa8312**.